Submesoscale tidal eddies in the wake of coral islands and reefs

Satellite data and numerical modelling

Delandmeter, Philippe; Lambrechts, Jonathan; Marmorino, George O.; Legat, Vincent; Wolanski, Eric; Remacle, Jean-François; Chen, Wei; Deleersnijder, Eric

DOI
10.1007/s10236-017-1066-z

Publication date
2017

Document Version
Accepted author manuscript

Published in
Ocean Dynamics: theoretical, computational oceanography and monitoring

Citation (APA)
Delandmeter, P., Lambrechts, J., Marmorino, G. O., Legat, V., Wolanski, E., Remacle, J.-F., Chen, W., & Deleersnijder, E. (2017). Submesoscale tidal eddies in the wake of coral islands and reefs: Satellite data and numerical modelling. *Ocean Dynamics: theoretical, computational oceanography and monitoring*, *67*(7), 897-913. https://doi.org/10.1007/s10236-017-1066-z

Published in "Ocean Dynamics"
year: 2017, volume: 67, pages: 897-913
doi: 10.1007/s10236-017-1066-z

Submesoscale tidal eddies in the wake of coral islands and reefs: satellite data and numerical modelling

Philippe Delandmeter · Jonathan Lambrechts · George O. Marmorino · Vincent Legat · Eric Wolanski · Jean-François Remacle · Wei Chen · Eric Deleersnijder

Philippe Delandmeter
Université catholique de Louvain, Institute of Mechanics, Materials and Civil Engineering (IMMC)
Avenue Georges Lemaître 4, B-1348 Louvain-la-Neuve, Belgium
E-mail: philippe.delandmeter@uclouvain.be

J. Lambrechts
Université catholique de Louvain, Institute of Mechanics, Materials and Civil Engineering (IMMC)
Avenue Georges Lemaître 4, B-1348 Louvain-la-Neuve, Belgium

G.O. Marmorino
Remote Sensing Division, Naval Research Laboratory
Washington, DC 20375, USA

V. Legat
Université catholique de Louvain, Institute of Mechanics, Materials and Civil Engineering (IMMC)
Avenue Georges Lemaître 4, B-1348 Louvain-la-Neuve, Belgium

E. Wolanski
TropWATER & College of Marine and Environmental Sciences, James Cook University
Townsville QLD 4811, Australia

J-F. Remacle
Université catholique de Louvain, Institute of Mechanics, Materials and Civil Engineering (IMMC)
Avenue Georges Lemaître 4, B-1348 Louvain-la-Neuve, Belgium

W. Chen
Remote Sensing Division, Naval Research Laboratory
Washington, DC 20375, USA

E. Deleersnijder
Université catholique de Louvain, Institute of Mechanics, Materials and Civil Engineering (IMMC) & Earth and Life Institute (ELI)
Avenue Georges Lemaître 4, B-1348 Louvain-la-Neuve, Belgium

E. Deleersnijder
Delft University of Technology, Delft Institute of Applied Mathematics (DIAM)
Mekelweg 4, 2628CD Delft, The Netherlands

Abstract Interaction of tidal flow with a complex topography and bathymetry including headlands, islands, coral reefs and shoals create a rich submesoscale field of tidal jets, vortices, unsteady wakes, lee eddies and free shear layers, all of which impact marine ecology. A unique and detailed view of the submesoscale variability in a part of the Great Barrier Reef lagoon, Australia, that includes a number of small islands was obtained by using a "stereo" pair of 2-m resolution visible-band images that were acquired just 54 seconds apart by the WorldView-3 satellite. Near-surface current and vorticity were extracted at a 50-m resolution from those data using a cross-correlation technique and an optical-flow method, each yielding a similar result.

The satellite-derived data are used to test the ability of the unstructured-mesh, finite-element model SLIM to reproduce the details of the currents in the region. The model succeeds in simulating the large scale (> 1 km) current patterns, such as the main current and the width and magnitude of the jets developing in the gaps between the islands. Moreover, the order of magnitude of the vorticity and the occurrence of some vortices downstream of the islands are correctly reproduced. The smaller scales (< 500 m) are resolved by the model, although various discrepancies with the data are observed. The smallest scales (< 50 m) are unresolved by both the model and image-derived velocity fields.

This study shows that high-resolution models are able to a significant degree to simulate accurately the currents close to a rugged coast. Very high-resolution satellite oceanography stereo images offer a new way to obtain snapshots of currents near a complex topography that has reefs, islands and shoals, and is a potential resource that could be more widely used to assess the predictive ability of coastal circulation models.

Keywords Submesoscale eddies · High resolution satellite imagery · SLIM · Unstructured mesh

1 Introduction

Tidal flows have been studied for decades, from global (Lyard et al., 2006; Carrere et al., 2015) to small scales such as narrow fjords or straits (Eliassen et al., 2001). While the main processes controlling the tidal dynamics are globally understood, it is still challenging to simulate correctly the tidal currents in regions with a complex bathymetry. Sea surface elevation is generally not extremely sensitive to the details of the model (Thomas et al., 2014), but modelling satisfactorily the velocity field is much more challenging. Furthermore, it is precisely the velocity that affects the transport and fate of waterborne particles of interest to environmental implications, such as plastic debris (Critchell and Lambrechts, 2016), fine sediment (Lambrechts et al., 2010; Delandmeter et al., 2015), turtle hatchlings (Hamann et al., 2011) and fish and coral larvae (Wolanski and Kingsford, 2014; Thomas et al., 2014; Wolanski, 2016).

For various ecological applications, it is then crucial to model the different phenomena generated by the tides. Tidal currents occur over a wide range of space and time scales, from a few metres to hundreds of kilometres and from a few seconds to various weeks (Wolanski et al., 2003; Lambrechts et al., 2008). Submesoscale processes and features such as vortices, free-shear layers and jets in

the wake of small islands or reefs affect significantly the transport of tracers and particles (Wolanski et al., 1984, 1996; Lambrechts et al., 2008; Mantovanelli et al., 2012; Wolanski and Elliott, 2015). Typically, the submesoscale eddies observed have a size varying from 10-20 m, which last a few minutes at most, to a about 1 km, which live a for few hours until the tide reverses.

The Great Barrier Reef (GBR) lies on the north-eastern continental shelf of Australia (Fig. 1a). It contains over 2500 reefs, in a band 2600 km long and 200 km wide. The topography and bathymetry of the region is complex and controls the tidal circulation. The zone of islands shown in Fig. 1d has an area of 13.5 km $\times$ 9.3 km and is the focus of the present study.

To model accurately the complex tidal currents in such regions, high-resolution models are necessary (Wolanski et al., 2003). Falconer et al. (1986) studied the model sensitivity to the bathymetry representation, for which a high resolution is then crucial; Coutis and Middleton (2002) highlighted the importance of the island geometry on controlling the wake formation downstream this island; Munday et al. (2010) went even further showing the potential of adaptive models. The simulation of such complex flows is now frequently done using finite element models, such as FINEL 2D (Dam et al., 2007), TELEMAC (Jones and Davies, 2008) or SLIM (Lambrechts et al., 2008). The key feature of these models is the possibility to deal with unstructured meshes. They allow for a correct representation of a complex bathymetry with narrow straits and gaps, small islands or reefs (Legrand et al., 2006; Lambrechts et al., 2008). Furthermore, they give the possibility to significantly increase the resolution in regions of interest (Hanert, 2004). SLIM[1] has been used extensively in the GBR hydrodynamics modelling (Lambrechts et al., 2008, 2010; Hamann et al., 2011; Thomas et al., 2014, 2015; Delandmeter et al., 2015; Critchell and Lambrechts, 2016; Grech et al., 2016).

Validation of such models has been attempted in a limited way, and over relatively small areas, through the use of current-meter and sea-level moorings (Thomas et al., 2014) and HF radar (Young et al., 1994). The use of satellite imagery for direct validation of a modelled velocity field is hampered by relative low spatial resolution (of the order of 1 km) and a typically long time interval between repeat views of a scene. For example, MODIS (Moderate Resolution Imaging Spectroradiometer) ocean color imagery from the Terra and Aqua satellites has $\sim$1 km resolution and a repeat interval of about 3 h (`modis.gsfc.nasa.gov`), which is longer than the time scale of the dominant M2 tide. At the other end of the spectrum of satellite imagery resolution are the WorldView-2 and -3 satellites (`http://www.digitalglobe.com/about/our-constellation`), which have very high-resolution imagery (2-m pixels for color imagery) and a repeat interval of the order of 1 min for those cases where data are collected in "along-track stereo" mode. Data collected in that mode are typically used to construct digital elevation models of land features, and rarely does one find a case revealing oceanographic phenomena.

The objective of the present study is thus two-fold: to examine the utility of high-resolution data and the predictive capability of a state-of-the-art coastal model to predict submesoscale features. Section 2 details the satellite images used and how they were processed by means of both a Particle Image Velocimetry (PIV) method and an optical-flow method, the so-called Global Optimal Solution (GOS),

[1] Second-generation Louvain-la-Neuve Ice-ocean Model (`www.climate.be/slim_flyer`)

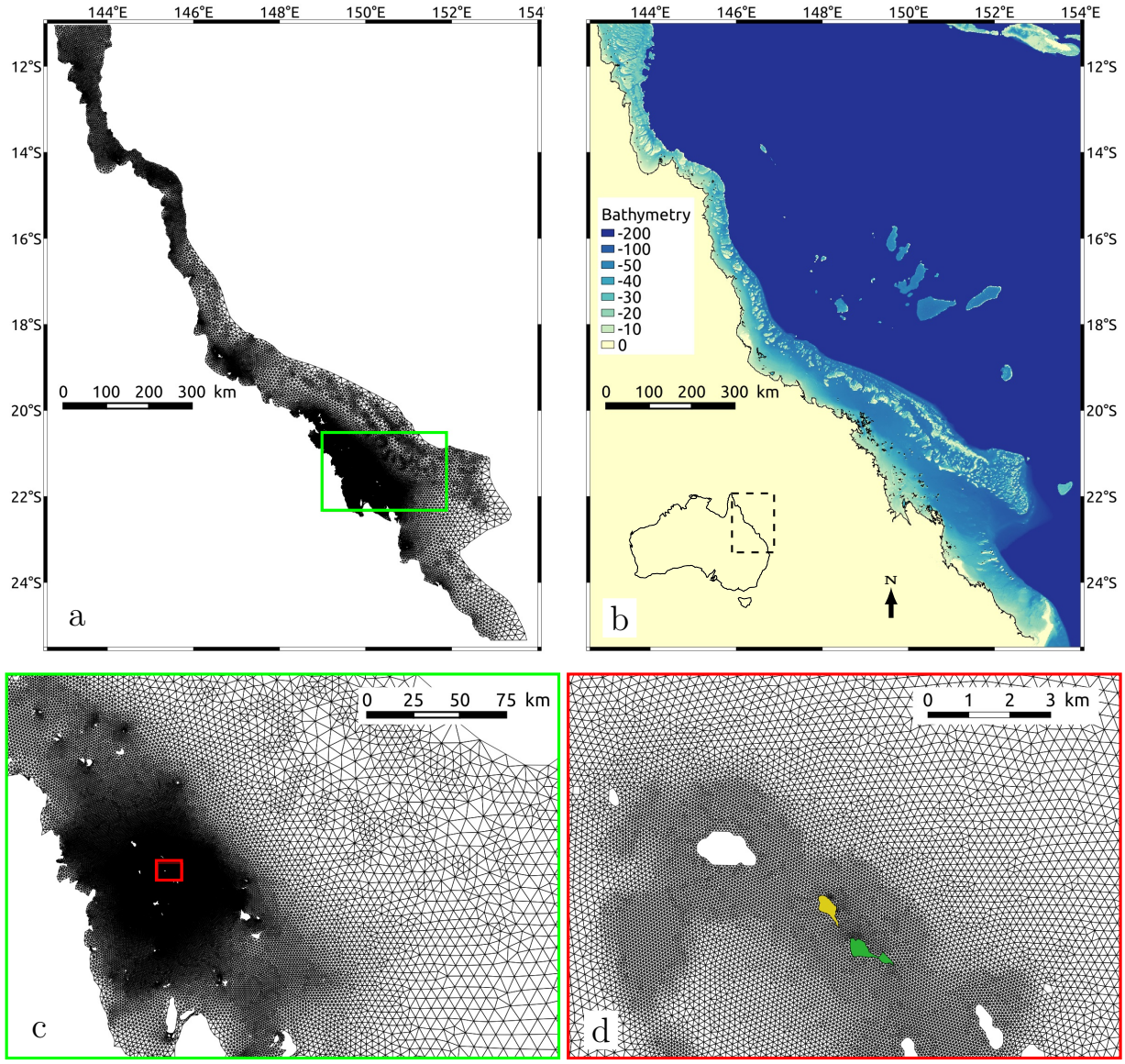

Fig. 1 Great Barrier Reef mesh (a,c,d) and bathymetry (d). The mesh used by the model SLIM to simulate the submesoscale processes around Beverlac (in yellow) and Hull (in green) Islands is composed of ∼110,000 DG triangles and its size varies between 50 m and 20 km. The mesh covers the whole GBR lagoon. The 13.5 km × 9.3 km zoomed area (d) is the focus of the present study.

to compute velocity maps. It also defines the numerical model SLIM. Section 3 explains the submesoscale patterns evolution during the tidal cycle, it validates the satellite data processing and it describes the numerical simulation results. Those results are discussed in Section 4 where the skills of SLIM on submesoscale eddy simulations in a rugged bathymetry are evaluated, before concluding in Section 5.

2 Methods

2.1 Satellite data and velocity algorithms

WorldView-3 imagery of an area of the GBR lagoon was acquired on 27 February, 2015, at 0010 UTC (10:10AM local time). The imagery consists of an in-line stereo pair, having a time interval between the two images of just 54 s. The data from each image has a spatial resolution of 2 m in each of eight visible and near-infrared bands, and 0.5 m in a single panchromatic band. An inner-field area (Fig. 1d), containing many complex submesoscale patterns, was chosen for the detailed study. Colour-stretched versions of the inner-field area, shown in Fig. 2, emphasize patterns of re-suspended sediment (bright-blue areas) and near-surface aggregations of algae (white filaments). The algae in the study are most likely the cyanobacteria *Trichodesmium* as it is common to the study area and the only algae to form locally large-scale, dense surface aggregations (Furnas, 1992; McKinna et al., 2011; McKinna, 2015). Extensive aggregations of *Trichodesmium* are most favoured in warm water and during extended periods of calm winds. Over the 10 h prior to the satellite acquisition, wind speeds measured near the study area were less than 3 m s^{-1}, and water temperatures were above 28.4°C. There were no nearby measurements of stratification, but the water column is generally well mixed (Furnas, 1992; Wolanski, 1994). Flow towards the north-east can be inferred from linear sediment bands in the gaps between islands, connecting to large downstream vortices, and giving the appearance of large "mushroom" shapes. White areas in the images are clouds, and adjacent dark areas are cloud shadows. The azimuth viewing angle is necessarily different for the two images (332° vs 271°); note the larger distance between clouds and their shadows in Fig. 2 (t_1 image). And, because of parallax, the location of a cloud in one image is considerably different in the other; the net effect being that the total area contaminated by clouds is approximately doubled when both images are considered together.

Velocity maps were extracted from those images using both a PIV technique and a GOS method, which are described below. To account for contamination by clouds and cloud shadows, as well as by a small amount of boat traffic, a mask was manually created to remove contaminated pixels from the velocity calculations. As the processing tools uses only gray-scale imagery, a single color wavelength band needed to be chosen for analysis. The yellow band was used (wavelength range of 590 to 630 nm), as this was judged to have the best signal-to-noise ratio for sediment and algae patterns.

2.1.1 Particle Image Velocimetry (PIV) method

Currents are derived from the stereo image pairs using a normalized cross-correlation algorithm (Tseng et al., 2012), which is implemented as a PIV "plugin" to the

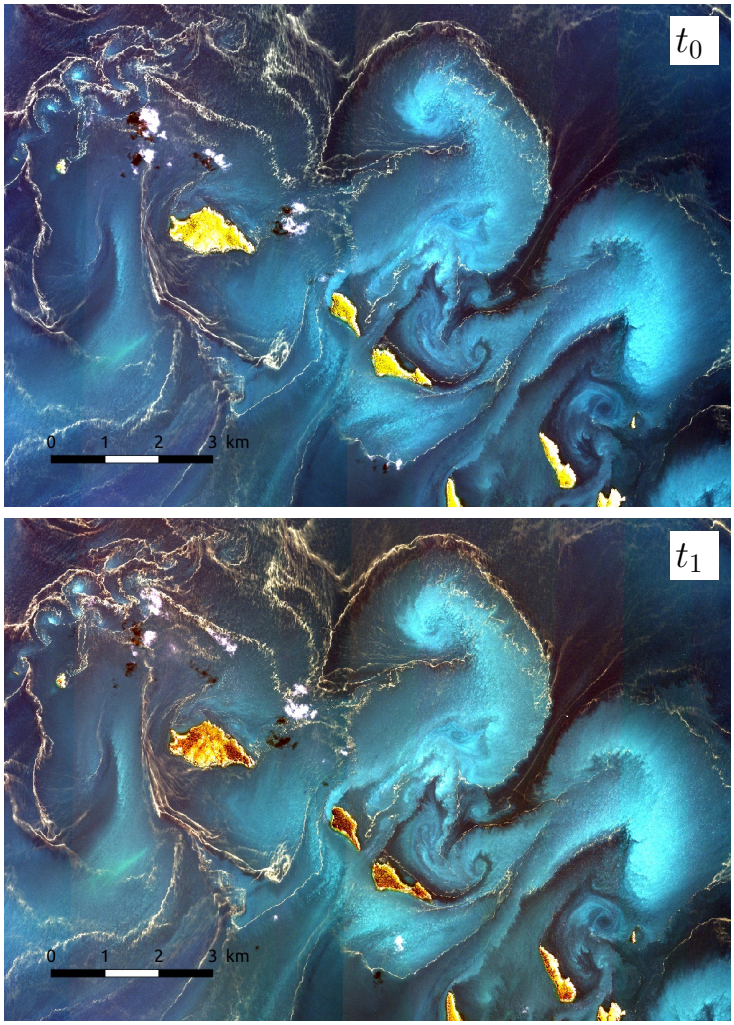

Fig. 2 WorldView-3 satellite imagery acquired on 27 February, 2015, at 0010 UTC (10:10AM local time). The t_0 picture was taken 54 s before the t_1 one. Shown are color-stretched versions, using red, green, and blue wavelength bands.

ImageJ processing and analysis package (https://imagej.nih.gov/ij/). In this algorithm an $n \times n$ pixel-sized interrogation window in the t_1 image is compared against a larger search area in the t_2 image. The difference in center positions of the interrogation window and its best match within the search area is then selected as the displacement vector; the displacement vector divided by the time step yields the velocity vector. A threshold (0.6, in this study) is used to distinguish high from low image correlations; a low correlation, resulting from a small interrogation window presenting insufficient features (or, image "texture"), which tends to yield an erroneous vector, can thus be easily filtered out and replaced by an interpolated value. Each successive interrogation window is displaced in the x

and y directions by $n/2$ pixels; the resulting velocity vectors thus have a physical spacing equal to $n/2 \times 2$ m. In the present study, $n = 64$, so that the velocity maps have a resolution of 64 m. Higher resolutions maps were computed, obtaining consistent results with the one shown in this paper, but they were contaminated by noise related to artefacts in the satellite imagery and are not shown in this paper.

2.1.2 Global Optical Solution (GOS) method

The GOS method (Chen, 2011) uses the conservation of a passive tracer to compute the velocity field. It assumes that the total (Lagrangian) derivative of the tracer is equal to zero for a short time interval, as represented by the following integrated form of the tracer-conservation equation:

$$I(\boldsymbol{r} + \boldsymbol{u}\Delta t, t_1) = I(\boldsymbol{r}, t_0), \tag{1}$$

where I is tracer intensity, $\Delta t = t_1 - t_0$ is the time difference between the two images and $\boldsymbol{r}$ and $\boldsymbol{u}$ are the position and velocity vectors at t_0 for a particular image pixel. The solution for $\boldsymbol{u}$ is an under-constrained problem. To tackle it, $\boldsymbol{u}$ is computed on a relative coarse grid and bi-linearly interpolated on all the pixels. In the present application, the coarse grid spacing is 200 m, while the pixel size is 2 m. The velocity $\boldsymbol{u}$ is eventually derived as the result of a non-linear optimization problem, minimizing the error in Equation 1. In this study, the tracer is the intensity of light scattered from re-suspended sediment and near-surface algae. These materials do not necessarily provide a passive tracer, because it is possible for the intensity to vary with angle of view. Sun glint can affect both GOS and PIV calculations; fortunately, good view angles coupled with a low sea state resulted in minimal contamination.

Note that each method (PIV and GOS) requires suitable small-scale "texture", or trackable features, to derive valid estimates of velocity and vorticity; and each may fail in areas having poor texture.

2.2 Numerical modelling

2.2.1 SLIM

The Second-generation Louvain-la-Neuve Ice-ocean Model (SLIM), a discontinuous Galerkin finite element model for shallow waters (Lambrechts et al., 2008; Thomas et al., 2014; Critchell et al., 2015; Le Bars et al., 2016), was used to simulate the hydrodynamics of the region. The main feature of the finite element method is the possibility to deal with unstructured meshes. This is particularly important to model the GBR, which is characterized by a complex topography and strong velocity gradients. Fig. 1 shows the mesh used by SLIM for this study. Even though the simulation focuses on the inner-field area, the mesh includes all of the GBR lagoon. The eastern boundary was defined as the 200 m isobath, which corresponds to the shelf break. The mesh resolution was increased close to the coast, the reefs and in the region of interest, with a size varying between 50 m and 20 km, to generate a final grid of ∼110,000 triangles. The 50 m mesh resolution in the inner-field was chosen to be comparable to the PIV and GOS data resolution.

The two-dimensional version of SLIM solves the depth-averaged shallow water equations, to compute the water elevation η and the depth-averaged current velocity $\boldsymbol{u} = (u, v)$:

$$\frac{\partial \eta}{\partial t} + \boldsymbol{\nabla} \cdot (H\boldsymbol{u}) = 0, \tag{2}$$

$$\frac{\partial \boldsymbol{u}}{\partial t} + (\boldsymbol{u}\boldsymbol{\nabla}) \cdot \boldsymbol{u} = -g\boldsymbol{\nabla}\eta - f\boldsymbol{e}_z \wedge \boldsymbol{u} - C_D|\boldsymbol{u}|\boldsymbol{u} + \frac{\boldsymbol{\tau}}{\rho H} + \frac{1}{H}\boldsymbol{\nabla} \cdot \Big(H\nu(\boldsymbol{\nabla}\boldsymbol{u} + \big(\boldsymbol{\nabla}\boldsymbol{u}\big)^T\Big)\Big),$$

where H is the total water column height and the physical parameters g, f, ρ and $\boldsymbol{\tau}$ are the gravitational acceleration, the Coriolis parameter, the density and the surface wind stress, respectively. $\boldsymbol{e_z}$ is the vertical unit vector pointing upward, $\wedge$ is the vector product operator and the superscript T stands for the transpose matrix operator. The bottom friction is parameterised as a quadratic expression, with the parameters:

$$C_D = g/(C^2 H), \quad C = H^{1/6}/n. \tag{3}$$

C and n are called the Chezy and the Manning coefficients, respectively. The eddy viscosity ν is obtained from the Smagorinsky parameterisation (Smagorinsky, 1963; Pham Van et al., 2014):

$$\nu = \alpha \Delta_x^2 \sqrt{2\left(\frac{\partial u}{\partial x}\right)^2 + 2\left(\frac{\partial v}{\partial y}\right)^2 + \left(\frac{\partial u}{\partial y} + \frac{\partial v}{\partial x}\right)^2}, \tag{4}$$

with α a non-dimensional coefficient and Δ_x^2 the local mesh size. The model setup used for the simulation is identical to that of Thomas et al. (2014), with $\alpha = 0.01$ and $n = 2.5 \times 10^{-2}$ s m$^{-1/3}$. Moreover, C_D is multiplied by a factor of 10 over shallow reefs.

2.2.2 Bathymetry

The bathymetry data used comes from the Project 3DGBR dataset v4 (Beaman, 2010), and has a resolution of 100 m (Fig. 1). This 4th version shows various differences comparing to the 3rd version, used in Thomas et al. (2014) and Delandmeter et al. (2015). The bathymetry was smoothed in such a manner that it does not vary from more than 50% between two nodes of an element. This smoothing operation preserves better the original bathymetry than diffusion operators used in previous studies. The error introduced by the smoothing operation is smaller than 20% on more than 88% of the domain. This error is mainly introduced close to the reefs far away from the region of interest, where the mesh size is large. In the inner-field region, shown on Fig 3, the error is smaller than 0.1% on more than 99% of the domain.

2.2.3 Open boundaries

The open boundaries are the interface between the GBR and the Coral Sea (Fig. 3), and these were forced with tides using the OSU TOPEX/Poseidon Global Inverse Solution TPXO 7.2 dataset (Egbert and Erofeeva, 2002; Delandmeter et al.,

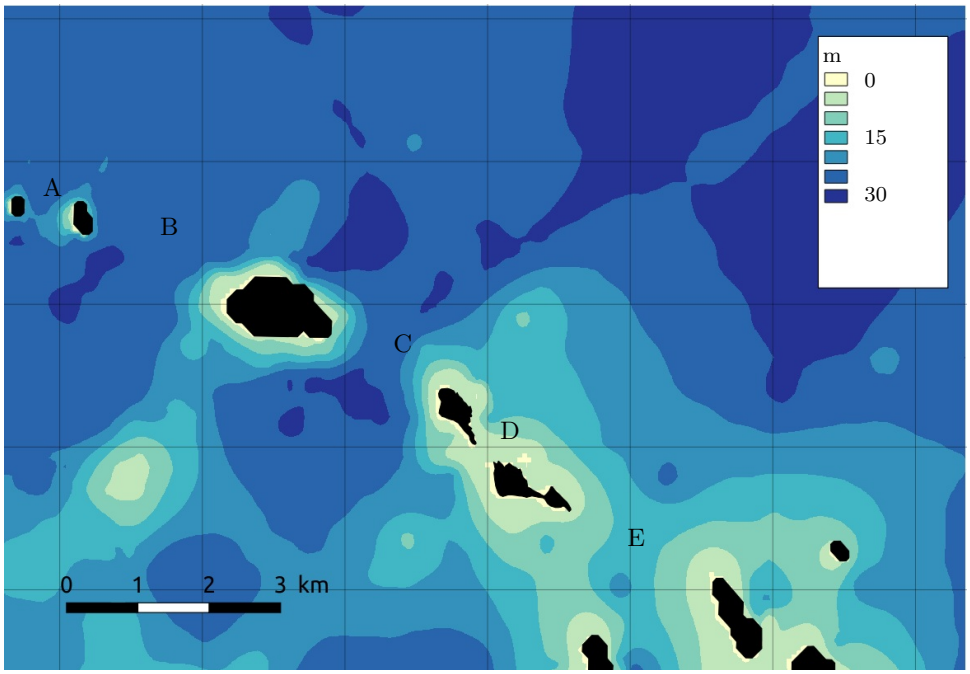

Fig. 3 Bathymetry used for the numerical simulation. The map displays the inner-field area, which corresponds to Fig. 1d. The full bathymetry is also displayed in Fig 1b. This inner-field area is used for all the results displayed in the following figures. The gaps between the different islands are tagged with letters from A to E.

2015), with a spatial resolution of 0.25°. Furthermore, the East Australian Current was accounted for by imposing a constant flow between 15.0°S and 17.6°S, as in Thomas et al. (2014).

2.2.4 Wind

Wind data, having a temporal resolution of 6 h and a spatial resolution of $0.3° \times 0.3°$, were obtained from the NCEP Climate Forecast System Reanalysis (Saha et al., 2010)). The wind was weak between February 20th and 27th, with an average speed of 7.3 m s^{-1}. The wind speed was smaller than the average speed more than half of the time. It blew at more than 12 m s^{-1} during 9% of the time, with a maximum speed of 15 m s^{-1}. Measurements at Hardy Reef and Heron Islands showed wind speeds less than 3 m s^{-1} over seven hours prior to the satellite overpass. Model results (not shown) that include wind forcing revealed that wind has no major influence on the velocity field; consequently, wind forcing was not used to obtain the results shown in this paper.

2.3 Analysis tools

To quantify the errors between PIV and GOS methods, a coefficient of determination r^2 is computed. To do so, in the inner-field region, the components $u_{//}$ and $u_{\perp}$ are defined as the flow aligned and perpendicular to the mean tidal flow, respectively. Then PIV and GOS data nodes are numbered from 1 to N. Defining the GOS velocities $u^i_{//}$ and $u^i_{\perp}$ and the PIV velocities $\hat{u}^i_{//}$ and $\hat{u}^i_{\perp}$, the coefficients of determination $r^2_{//}$ and $r^2_{\perp}$ read:

$$\begin{aligned}
\bar{u}_{//} &= \frac{1}{N}\sum_{i=1}^{N} \hat{u}^i_{//} & \bar{u}_{\perp} &= \frac{1}{N}\sum_{i=1}^{N} \hat{u}^i_{\perp} \\
\mathrm{SSE}_{//} &= \sum_{i=1}^{N} \left(u^i_{//} - \hat{u}^i_{//}\right)^2 & \mathrm{SSE}_{\perp} &= \sum_{i=1}^{N} \left(u^i_{\perp} - \hat{u}^i_{\perp}\right)^2 \\
\mathrm{SST}_{//} &= \sum_{i=1}^{N} \left(\bar{u}_{//} - \hat{u}^i_{//}\right)^2 & \mathrm{SST}_{\perp} &= \sum_{i=1}^{N} \left(\bar{u}_{\perp} - \hat{u}^i_{\perp}\right)^2 \\
r^2_{//} &= 1 - \frac{\mathrm{SSE}_{//}}{\mathrm{SST}_{//}} & r^2_{\perp} &= 1 - \frac{\mathrm{SSE}_{\perp}}{\mathrm{SST}_{\perp}}.
\end{aligned} \tag{5}$$

SSE and SST are the sum of squared error and the sum of squared total, respectively. The closer r^2 to unity, the better the matching.

As there are only two satellite images, only a single velocity "snapshot" could be constructed. It is then impossible to follow the path of particles during a tidal cycle. To compare simulation results and data, velocity is assessed comparing "instantaneous streamlines" obtained from data and from the velocity field at the same instant. The vertical component of the relative vorticity, defined as $\zeta = \partial v/\partial x - \partial u/\partial y$, is also computed. Throughout this paper, it will be referred to as vorticity, for simplicity.

3 Results

3.1 Parameter sensitivity

The model is sensitive to its parameters. In this study, those parameters were chosen identical to Thomas et al. (2014). The parameters for the bottom friction and the eddy diffusivity are:

$$n = 2.5 \times 10^{-2}\ \mathrm{s\ m^{-1/3}}, \quad \alpha = 10^{-2}. \tag{6}$$

In preliminary simulations, the sensitivity to those parameters was evaluated. Increasing by a factor 3 the Manning coefficient (n) reduces by 1/3 the jet speeds in the inner-field, contributing to a large decrease of the submesoscale activity. A similar result is obtained by increasing the eddy viscosity parameter (α) by a factor 100.

3.2 Summary of the tidal cycle

The GBR hydrodynamics was simulated for eight days, starting on February 20th, 2015. Fig. 4 shows the dynamics in the inner-field region during part of the tidal cycle, on February 26th and 27th. At 1930 UTC, the tidal currents reversed and began to propagate towards north-east. The current strength increased and vortices developed on both sides of each jet. The jets were the strongest around 2230 UTC then began to weaken, but vortices still developed, even when the tidal current reversed (0230 UTC to 0330 UTC). They were then dissipated while the tide began to propagate in the opposite direction (0430 UTC) in a new half a cycle.

3.3 Coefficients of determination and scatterplots

Velocities computed by the PIV and GOS methods are closely matched. The coefficients of determination obtained are:

$$r^2_{//} = 0.926, \qquad r^2_{\perp} = 0.913. \tag{7}$$

The coefficient of determination is a good tool to compare PIV and GOS methods which process the same data, i.e. the same patterns. However, it cannot be used to compare two datasets in which there is a possible space shift between the patterns, as it is the case when comparing SLIM and data. SLIM results give a negative value for both $r^2_{//}$ and $r^2_{\perp}$. According to the r^2 method, it means that SLIM is worse than simply computing the averaged velocity over the domain, which by construction gives $r^2 = 0$. This simply illustrates how the method cannot be used to compare datasets with possible shift, although it works fine to compare PIV and GOS methods.

PIV, GOS and SLIM results are also compared through the use of scatterplots. Fig. 5 shows an example for the parallel flow component. The PIV/GOS comparison gives almost a perfect match, which is not unexpected as those estimates derive from the same image data. The PIV/SLIM comparison, however, is rather widely dispersed; this can derive from either actual errors in modelling or small spatial shifts between PIV and SLIM velocity patterns. The main information given by the PIV/SLIM scatterplot is the $\sim$0.1 m s^{-1} shift in the flow parallel component. There are a number of possible explanations for this discrepancy. One of them is the use of an incorrect bottom stress coefficient. Another one is the vertical shear, which is missing from the two-dimensional approach: the vertically-averaged SLIM flow naturally underestimates the surface flow, since the vertical profile of the jet is logarithmic. Finally, an unseasonal increase in the South Equatorial Current or the influence of the Capricorn eddy in the Southern GBR, which is not included in the model (Kingsford and Wolanski, 2008; Mao and Luick, 2014), may affect the results.

Since PIV and GOS methods show the same patterns, only the PIV method results are compared to SLIM, for simplicity.

3.4 Wind effect on the PIV velocities

Because the color patterns detected by the satellite derive in part from material close to the sea surface, the possible extent of wind drift on the derived velocity

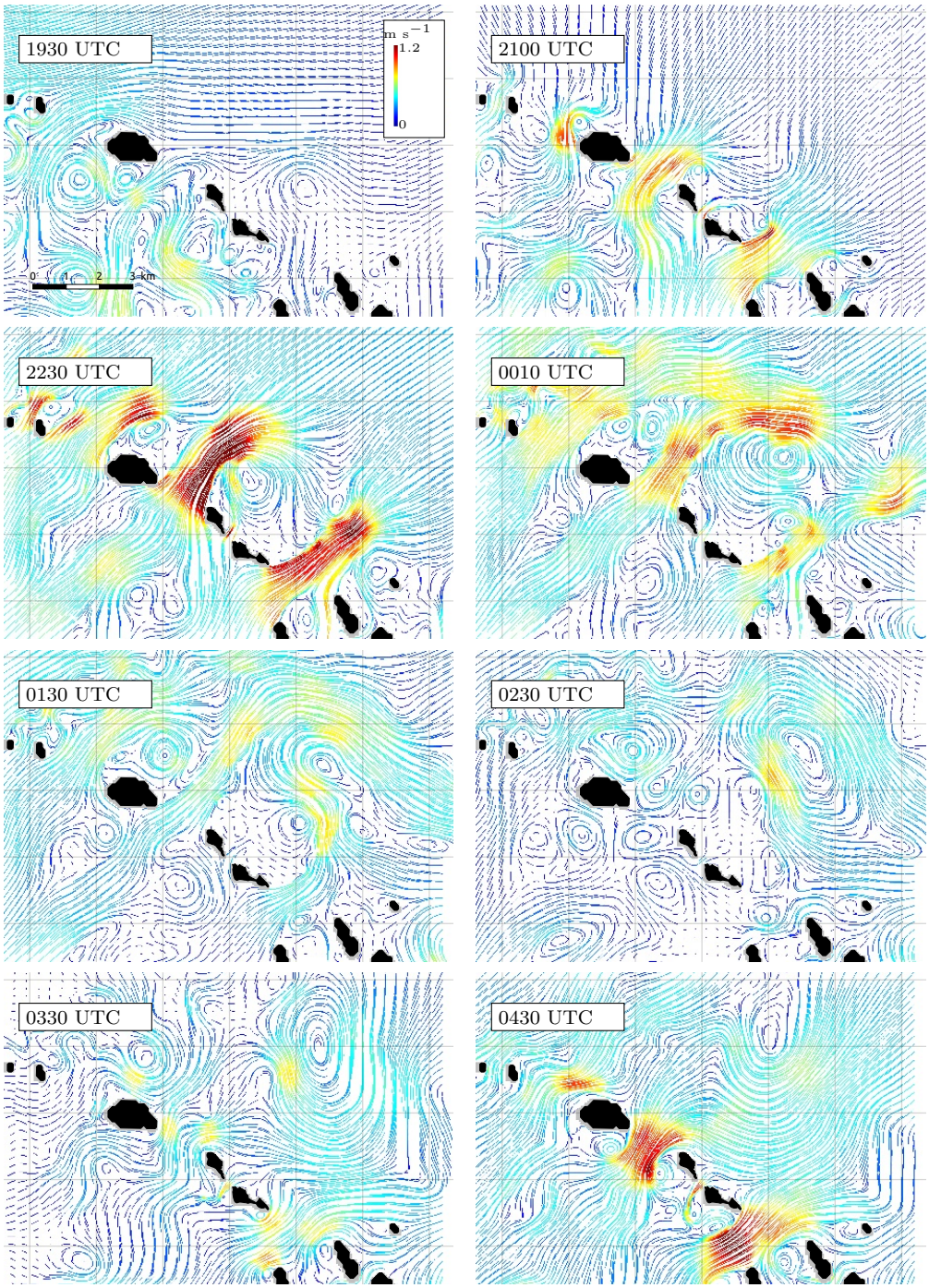

Fig. 4 Evolution of the tidal current in the inner-field region, from February 26th 1930 UTC until February 27th 0430 UTC.

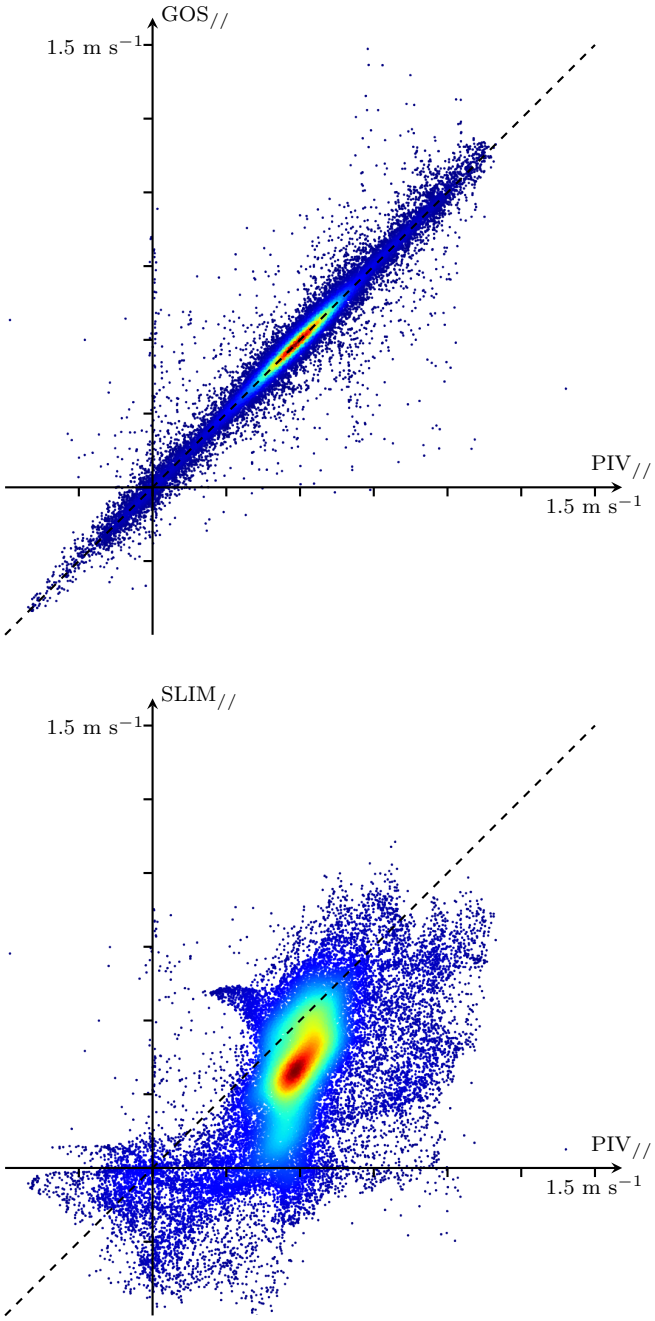

Fig. 5 Scatterplot comparing the parallel flow component of the PIV and GOS data (top panel) and PIV and SLIM data (bottom panel). While the PIV/GOS comparison gives almost a perfect match, the PIV/SLIM comparison is more dispersed. A shift is observed in the PIV/SLIM comparison. The colormap indicates the point density.

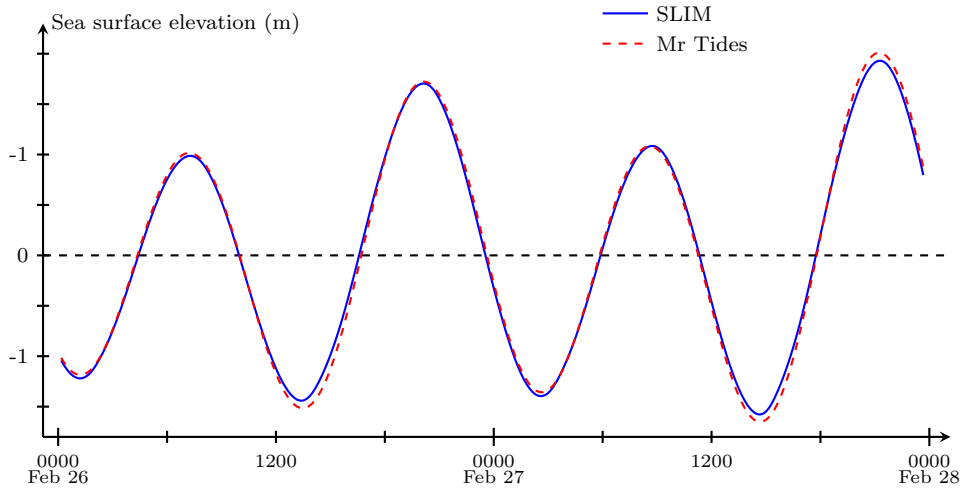

Fig. 6 Comparison between sea surface elevation from the Mr Tides software and SLIM results at Middle Island Anchorage station. The maximum relative error is 3.8%.

field should be considered. Fig. 10 from the appendix compares the result as given in Fig. 7 with the case for which there is a wind-drift current, defined as 2% of the wind velocity (Critchell and Lambrechts, 2016). The wind does not change the global dynamics, but the mean flow is rotated counter-clockwise by about 5°.

3.5 Sea surface elevation validation

The satellite provides no information about tidal elevation. To validate the tidal evolution over time, SLIM sea-surface elevation is compared to output from tidal prediction software (`www.mrtides.com`) at Middle Island Anchorage station (21°39'S, 150°15'E), which is located 42 km south-east of Hull Island. A comparison over four tidal cycles shows a maximum relative error of 3.8% (Fig. 6).

3.6 PIV and SLIM spatial comparison

Over the large scale, the main tidal current has the correct direction and speed, as observed upstream the islands. At smaller scales, however, some differences occur; for example, the vortices downstream of the islands tend to be larger in the model than in the data. Fig. 7 compares streamlines computed from the satellite data (PIV method) and from the SLIM results. The main patterns observed on the data (top map) are reproduced by the model: three large jets, developing from island-gaps B, C and E appear in both SLIM and PIV maps. The modelled jets widths are similar to the PIV jets; and the speeds are close, except for jet E, which is slower than in PIV data. Jet B is weaker and wider than the two others on both maps, although it is partially masked in the PIV map by the presence of clouds in the area (see Fig. 2).

The streamlines follow similar paths downstream of gap A and in the south-eastern corner of the maps, where small-scale vortices (diameters < 1 km) appear. However, many vortices observed in the model upstream of the islands are not present in the PIV map.

On the PIV map, jet D develops only $\sim$800 m downstream of gap D (see Fig. 7, top map), which is physically impossible. The jet is generated by the gap, it should start at the gap or even upstream of it, not downstream of it where there is nothing anymore to generate it. This error arises from a lack of trackable small-scale features in the region of the gap, presumably as the result of enhanced mixing throughout the water column in that shallow area. Jet D is essentially missing from the model. This may be the result of "upstream blocking" by the residual tidal eddies found in the model upstream of the Hull and Beverlac Islands.

Fig. 8 shows the vorticity as computed from PIV (top map) and SLIM (bottom map). The first observation is that the data vorticity magnitude within the free shear layers developing downstream of the different islands is reproduced by the model. The "vortex street" of cyclonic and anti-cyclonic vortices downstream of the two north-western islands (around gap A) is correctly reproduced by the model, with the correct vorticity magnitude, similar free shear layer width, and the embedded patterns. Those good results are also present in the south-eastern corner of the inner-field, but the widths of other free shear layers are not as accurate as in above-mentioned areas. While the different vortices downstream of gap C detach one from each other in the SLIM results, such activity is not apparent in the PIV map. Finally, as already observed with the streamlines maps, there is some submesoscale activity observed upstream of the islands in the model but not in the data. However, all the vortices observed in the model in this area are not absent from data. For example, the negative and positives vortices, located 3 km south of gap B also appear in the PIV data.

4 Discussion

4.1 Satellite data and processing

High-resolution satellite data were processed by both the PIV and GOS methods, leading to similar results. The completely different approach of the two methods and the similarity of the output inspires confidence in the results. However, regions with lack of suitable texture can be affected by a loss of accuracy, such as gap D. A jet should develop near the entrance to the gap, not only 800 m downstream (Fig. 7, top map). This is an example of a localized error. Elsewhere, the small-scale patterns of algae and re-suspended sediment enable the generation of a physically realistic velocity field.

4.2 Modelling

The quality of the simulation is evaluated through the comparison of the patterns observed on the streamlines and vorticity maps (Figs. 7 and 8). SLIM succeeds in globally reproducing the correct speeds of both the main flow and the jets, and vorticity patterns similar to those observed. One difference is found for the

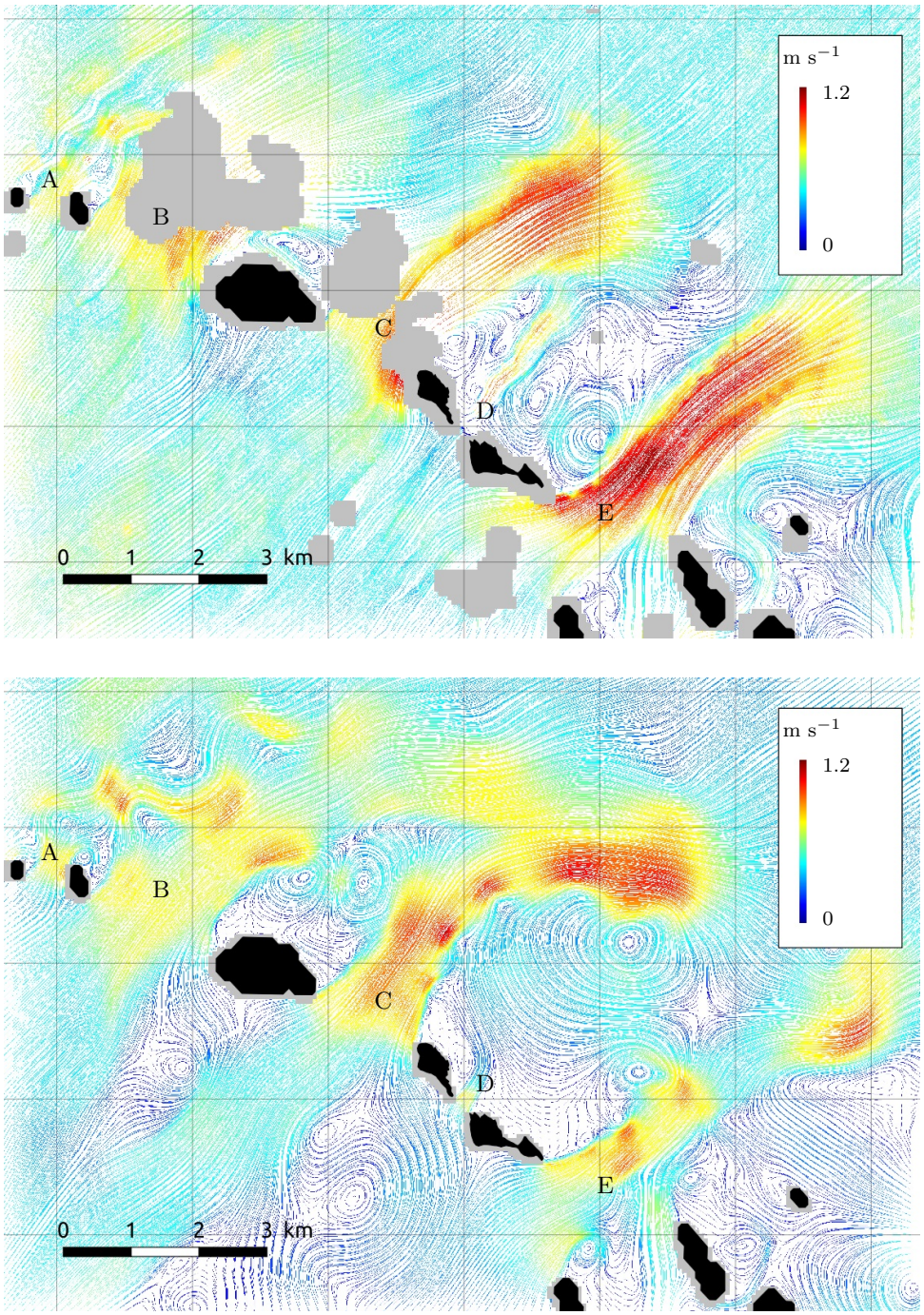

Fig. 7 Streamlines computed from the velocity field obtained with the PIV method (top map) and with SLIM (bottom map). Grey areas in the PIV map indicate where contaminating effects such as clouds are masked. Grey areas in the SLIM map result from the projection from the unstructured grid to the structured grid of PIV map. The color shows the magnitude of the velocity field.

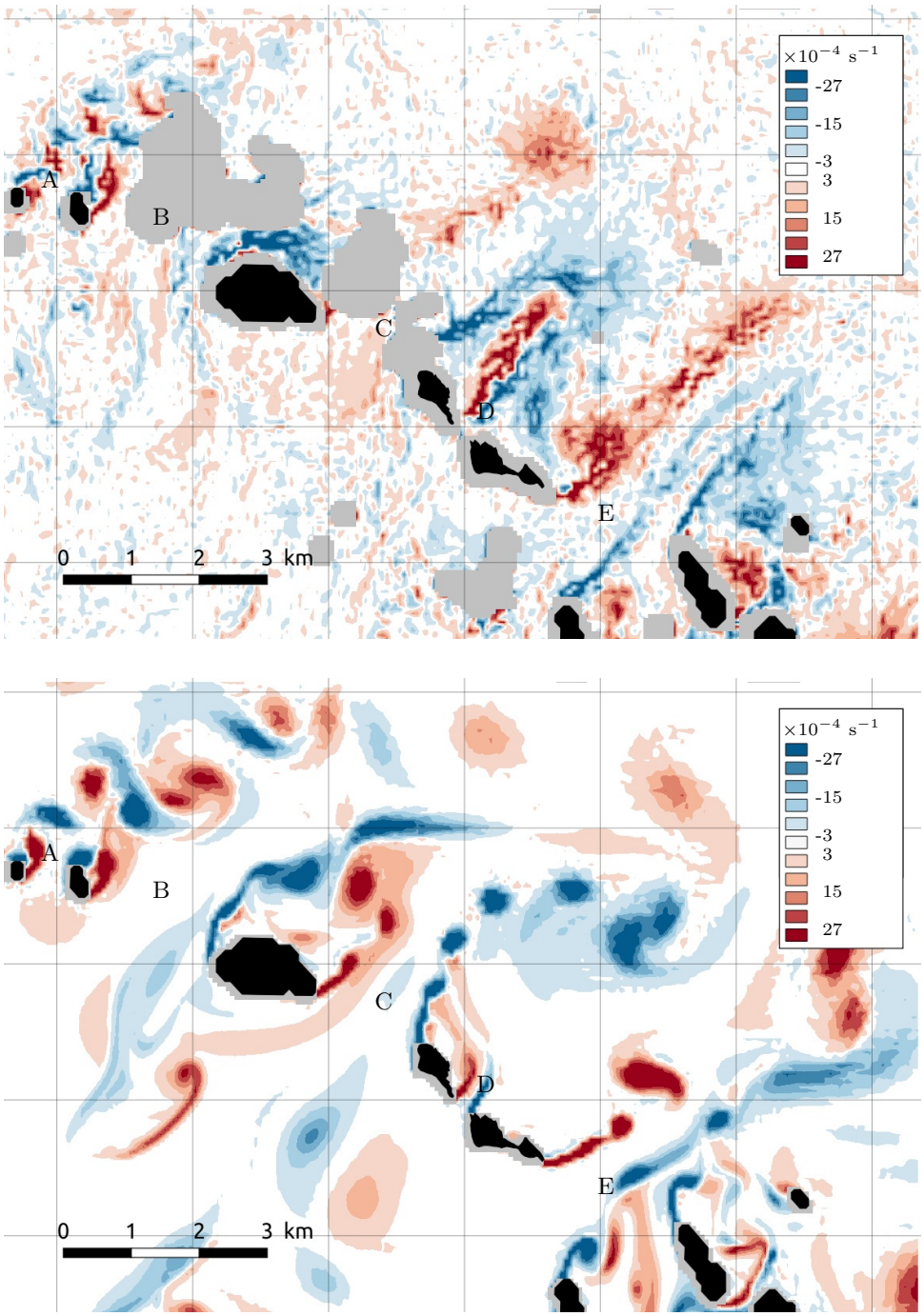

Fig. 8 Vorticity computed from the velocity field obtained with the PIV method (top map) and with SLIM (bottom map).

modelling of jet E. While in the data it is a constant speed large jet extending on ∼5 km, the jet speed is spatially oscillating in the model. This difference in behaviour might be the consequence of various factors. Firstly, the parameterisations of the unresolved smaller scales are not perfect. Secondly, the roughness of the sea floor, which has a large impact on the dynamics in shallow waters, is not known precisely. Thirdly, errors in bathymetry can drastically affect the jet speed. Jet E speed decreases suddenly 3 km downstream of gap E, before re-accelerating 1 km further away. This change corresponds to sudden changes in the bathymetry. But computing the transport conservation in the jet shows that the bathymetry variations are not sufficient to explain the jet speed oscillations. Eventually, the interactions between the jet and the surroundings vortices should be taken into account. In the PIV data, jet E is much (∼50%) stronger than in SLIM, its strength potentially prevents it from being affected by surroundings vortices while it is not the case for the modelled jet. The overall problem could then come from the jet being weaker since the beginning, at gap E.

Vortices are observed upstream of the islands in the SLIM results. Those vortices are generated by the bathymetry patterns in that area. Some of those appear in the PIV map, such as around the shallower area 3 km south of gap B, but other are missing completely. This difference could be a consequence of errors in the bathymetry input. Those vortices have a large importance, since they weaken the transport towards north-east, affecting the strength of jets D and E.

The vorticity inside the modelled free shear layers is unresolved. This result is not unexpected: besides the fact that the mesh size used prevents the model from resolving such small scales, those small size patterns are presumably non-hydrostatic and cannot be resolved by SLIM. However, even if the free shear layer is not fully resolved, it does not mean that the total vorticity flux is wrong, since the vorticity flux is not affected by the details in the free shear layer. It only depends on the velocity at the layer boundary. This result is detailed in Appendix A.

Despite the aforementioned differences, the model performs correctly to simulate the submesoscale patterns observed on PIV data. Indeed, the jets developing from the different gaps have globally the correct extent, width and speed, except jet E. The model is not too diffusive, since too large a diffusion would decrease the velocity gradient and show incorrect vorticity magnitudes, which is not the case in the model results. The model does represent correctly the main vortices on both sides of the jets developing from the different gaps. Fig. 7 shows that vortices do not appear at the same location at the same moment, and the vortex developing from gap D is much larger in the model than in the data. But the vorticity in the wake of an island is highly unsteady (see the modelled vortices evolution in Fig. 4), it would be hard to represent exactly the vortices size and timing.

4.3 Sub-grid scale processes and ecological impact

The satellite imagery reveals the presence of small eddies in the free shear layers (Fig. 11). Field and laboratory studies of free shear layers at other sites but at similar spatial scales, as well the analogy with field studies of the small eddies generated by phalarope swimming, suggest that small eddies of 10-20 m in diameter are continuously produced in the free shear layer and dissipated within a few minutes (Onishi and Nishimura, 1980; Onishi, 1984; Wolanski and Elliott, 2015).

These small eddies generate a very strong up-welling in their center, up to 0.1 m s^{-1} (Wolanski, unpublished data), and a strong down-welling along their outer edges and this increases the vertical eddy viscosity within the free shear layer; essentially the free shear layers provides a viscous outer boundary to the island wakes, thereby partially isolating them from waters on the outside. In turn, as shown by Wolanski et al. (1996), this generates an upwelling in the center of the island wake and a downwelling on the outer edges, while the strength of the eddy in the island wake is only slightly altered. The satellite images and the depth-averaged model are of course unable to assess the magnitude of the vertical motions.

The eddy-rich free shear layers, with a size varying from a few hundred metres to a few kilometres, have important ecological implications because they control the formation of patches of plankton, which can remain stable until the tide reverses (Hammer and Hauri, 1977). Also, the isolating effect of the free shear layers should decrease the export of waterborne larvae originating from the island and thus enhances self-recruitment (Nakano, 1957; Wolanski and Hamner, 1988; Signell and Geyer, 1991; Wolanski, 1993; Wolanski et al., 1996; Obst et al., 1996; White and Wolanski, 2008). The eddies present in the studied area are tidally generated and have a short lifespan, but their long-term implications are unknown. A starting point to address this last would be an understanding of the velocity field on the scale of the free shear layer eddies. So, one idea is to redo the analysis using the PAN imagery (zoom shown in Fig. 11), which has a spatial resolution of 0.5 m. The problem here is time resolution: the time-scale of the eddies is comparable to the image time interval of 54 s; thus, the velocity field on the scale of the smallest eddies cannot be obtained from existing imagery. It is suggested, therefore, that higher-resolution model studies, perhaps using idealized bathymetry, be performed to study how such eddy-rich shear layers may affect the ecology around islands and reefs.

A better understanding of the eddy and free shear layer dynamics could be obtained by comparing the eddies observed in this study with smaller scale engineering applications or larger scale geophysical studies. At a smaller scale, Huang et al. (1995) studied the wake dynamics downstream of a porous medium, similar to a set of various solid body wakes, such as the present multiple islands. The small eddies generated directly downstream of the porous medium interact and merge together further away, analogously to what is observed in Fig. 7. Other studies focused on the suppression of the vortices downstream of a solid body by the placement of a second body downstream of the first one (Strykowski and Sreenivasan, 1990; Sakamoto et al., 1991). Such a setting is similar to the small islands set in the south-eastern corner of the map in Figs. 7 and 9. At a larger scale, the interaction of multiple island wakes (Dong and McWilliams, 2007; Caldeira and Sangrà, 2012) is also important, where eddies generated by small islands lead to the destabilisation of the free shear layer of a neighbouring larger island. Smaller and larger scale applications have then many similarities and should not be neglected for a study of the wake dynamics.

5 Conclusions and perspectives

A unique pair of 2 m-resolution satellite images, taken only 54 seconds apart, was obtained in the central Great Barrier Reef. Using two different approaches, a cross-

correlation method (PIV) and an optical-flow method (GOS), a velocity field was obtained. It shows with a high resolution a rich submesoscale activity, including many small and large jets and vortices of different sizes. PIV and GOS methods give closely matching results, with however some errors in regions with lack of suitable texture, such as in the narrow gap between Beverlac and Hull Islands.

The unstructured-mesh, finite-element model SLIM was used to simulate the full Great Barrier Reef lagoon hydrodynamics, with an increased resolution, up to 50 m, in the Beverlac and Hull region (Fig. 1d). Results obtained are in overall agreement with the PIV and GOS data, even if discrepancies appear between the smallest-scale patterns. The global submesoscale activity, such as the extent, width and speed of the jets, and the magnitude of vortices at both sides of each jet and each island, is in accordance with PIV and GOS data. The model is not able to simulate exactly every single vortex position and size. It is concluded that these shortcomings must be related to the model assumptions and the accuracy of the forcing and bathymetry, both of which have a much coarser resolution than the size of the missed patterns.

High-resolution satellite images combined with the PIV or the GOS methods to build a velocity map are a new way to observe spatially complex submesoscale processes in shallow water regions. They also give much more information than current-meter and elevation moorings, for a much better validation of models. They are a potential resource that could be more widely used to assess the predictive ability of coastal circulation models. SLIM is generally successful in this validation, showing similar patterns to those in the satellite images

6 The way forward

This study has shown that a stereo-pair of high-resolution satellite images can capture the complexity of the flow around islands and reefs in shallow continental shelf water, that include jets, eddies, shear layers and stagnation zones. The satellite-derived velocity field was used to assess if oceanographic models are able to reproduce that complexity. To some degree the model is successful, but discrepancies occur. These are unlikely to be due to the two-dimensional modelling approach, as three-dimensional models do not simulate the phenomena any better (Wolanski et al., 2003). It is suggested that the lessons from engineering fluid mechanics may be useful here, including non-hydrostatic models; though even those models would not resolve all the complexity of this flow, especially if the resolution and the accuracy of the bathymetry and the forcing is not markedly increased. A better knowledge of the sea bed would also be necessary to improve the bottom-friction parameterisation. Significant improvement may only result from the assimilation of high-resolution field data, such as surface currents measured by a high-frequency radar. The limit will remain the parameterisation of sub-grid-scale eddies, even in the absence of islands or reefs (Robinson, 2012).

Acknowledgements

Computational resources were provided by the Consortium des Équipements de Calcul Intensif (CÉCI), funded by the Belgian Fund for Scientific Research (F.R.S-

FNRS) under Grant No. 2.5020.11. G. Marmorino was supported by NRL project 721C0-06; W. Chen by project 6778-06. E. Deleersnijder is an honorary research associate with the F.R.S-FNRS.

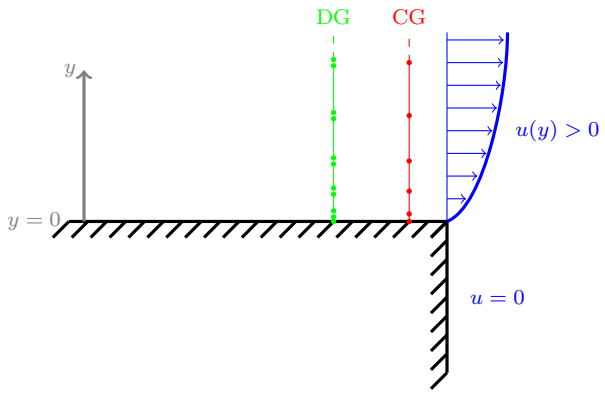

Fig. 9 Vorticity generated in a boundary layer. Simple 1D test case.

A Total vorticity flux in the free shear layer

In this section, it is shown that the total vorticity flux in the lee of a backward facing step computed using two different finite element methods, respectively a P1 continuous-Galerkin method and a P1 discontinuous-Galerkin method (such as SLIM), is insensitive to the numerical method and mesh resolution if computed correctly. This appendix is inspired from Deleersnijder (2016) and D.P. Marshall (2006, personal communication to E. Deleersnijder), who studied the sensitivity of the total vorticity flux to various finite difference numerical schemes, obtaining the same conclusions as for the finite element schemes detailed hereinafter.

Let assume a flow propagating alongside a wall (see Fig. 9), with a velocity u. This velocity is zero on the wall ($y = 0$). A boundary layer develops in the y-direction. The vorticity is $\omega = -\partial u/\partial y$ and the total vorticity flux is:

$$\Phi = \int_0^\infty u\ \omega\ dy = -\frac{u_\infty^2}{2}. \tag{8}$$

CG formulation

The 1D domain is discretized into linear elements. On element e, the two nodes are numbered e and $e+1$ and the finite element solution is $\hat{u} = \sum_{i=0}^{1} U_{e+i}\phi_i^e$, where ϕ_0^e and ϕ_1^e are the piecewise linear shape functions, equal to 0 everywhere except at node e and $e+1$, respectively. $\hat{\phi_0}$ and $\hat{\phi_1}$ are the shape functions on the parent element. The vorticity is defined as $\hat{\omega} = -\sum_{i=0}^{1} U_{e+i}\partial\phi_i^e/\partial y$. The vorticity flux $\hat{\Phi}$ is then:

$$\hat{\Phi} = -\sum_{e=0}^{\infty}\int_{\Omega_e} \hat{u}\frac{\partial\hat{u}}{\partial y}dy \tag{9}$$

$$= -\sum_{e=0}^{\infty}\int_{\Omega_e}\sum_{i=0}^{1}\sum_{j=0}^{1} U_{e+i}\phi_i^e\ U_{e+j}\frac{\partial\phi_j^e}{\partial y}dy \tag{10}$$

$$= -\sum_{e,i,j} U_{e+i}U_{e+j}\int_{\hat{\Omega}_e}\hat{\phi}_i\frac{\partial\hat{\phi}_j}{\partial\xi}d\xi \tag{11}$$

$$= -\sum_{e=0}^{\infty}\left(\frac{U_{e+1}^2}{2} - \frac{U_e^2}{2}\right) \tag{12}$$

$$= -\frac{U_\infty^2}{2}. \tag{13}$$

DG formulation

Again, the domain is discretized into linear elements. On element e, the two nodes are numbered $2e$ and $2e+1$. This time, the vorticity can not be defined as for the CG formulation, since the nodes are discontinuous at the element interfaces. This discontinuity has to be accounted for properly. On element e, vorticity W_{2e} and W_{2e+1} are computed resolving:

$$\sum_{j=0}^{1} W_{2e+j} \int_{\omega_e} \phi_j^e \phi_i^e dy = \sum_{j=0}^{1} U_{2e+j} \int_{\omega_e} \phi_j^e \frac{\partial \phi_i^e}{\partial y} dy - [u^* \phi_i], \qquad i = 0, 1. \tag{14}$$

The only way to obtain the correct vorticity flux is by defining the following u^* at the interfaces as the mean of the two nodal values:

$$u^* = \frac{U_{\text{top}} + U_{\text{bot}}}{2}, \tag{15}$$

where U_{top} and U_{bot} are the nodal values above and below the interface, respectively. Now the vorticity flux can be computed easily:

$$\hat{\Phi} = \sum_{e,i,j} U_{2e+i} W_{2e+j} \int_{\Omega_e} \phi_i^e \phi_j^e dy \tag{16}$$

$$= \sum_{e=0}^{\infty} \frac{1}{2} \big[- \big(U_{2e+1} U_{2e+2}\big) + \big(U_{2e-1} U_{2e}\big) \big] \tag{17}$$

$$= -\frac{U_\infty^2}{2}. \tag{18}$$

Provided that the velocity at the element interfaces is computed correctly and that the velocity outside the boundary layer is correct, the DG finite element method computes accurately the vorticity flux, even if the local velocity in the boundary layer is under-resolved or even wrong.

B Extra figures

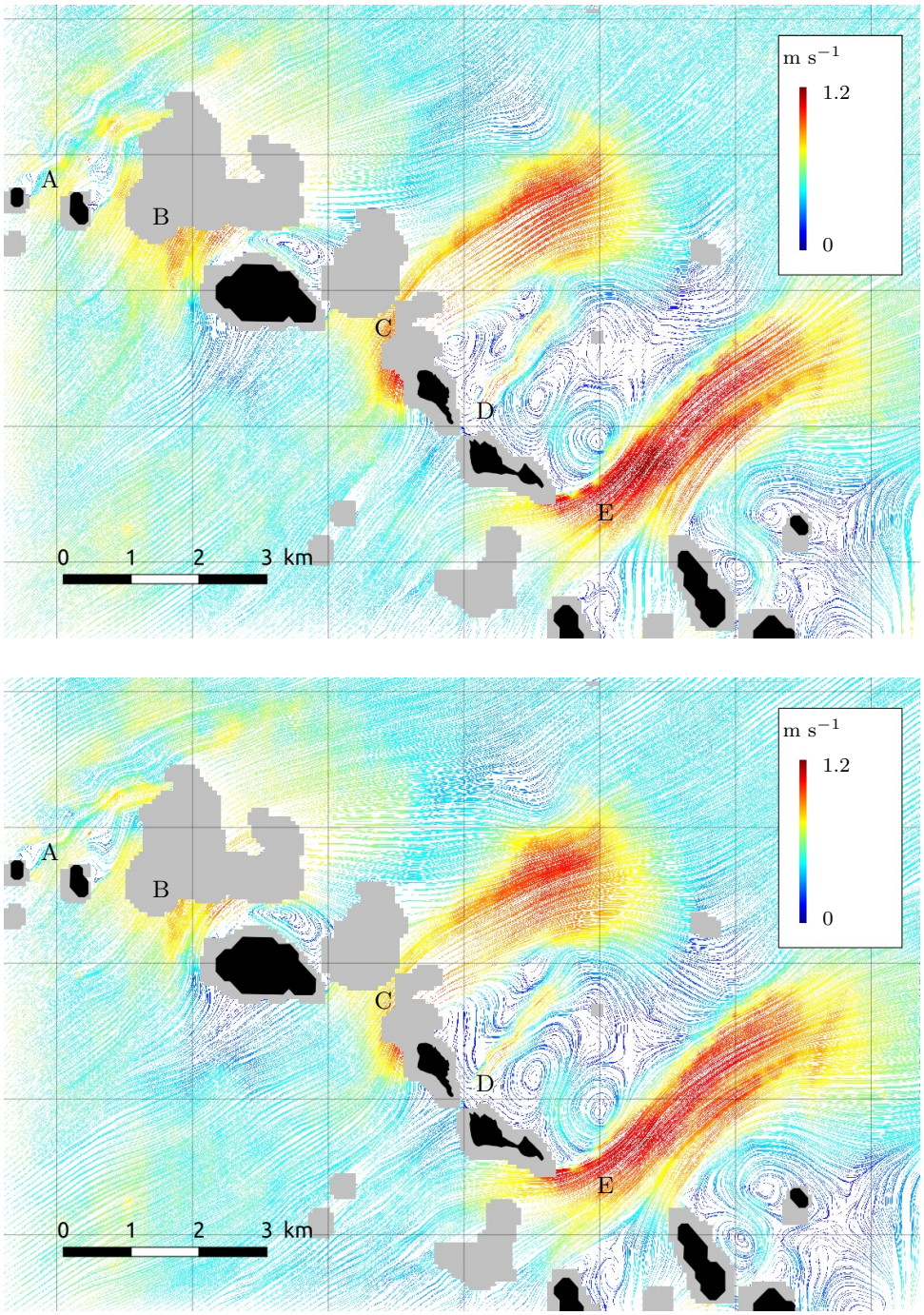

Fig. 10 Effect of a 2% wind shift on the velocity map of PIV data. While top map shows the original velocities computed with the PIV method (same as in Fig. 7), the bottom map removes a 2% contribution of the wind velocity to the PIV velocity.

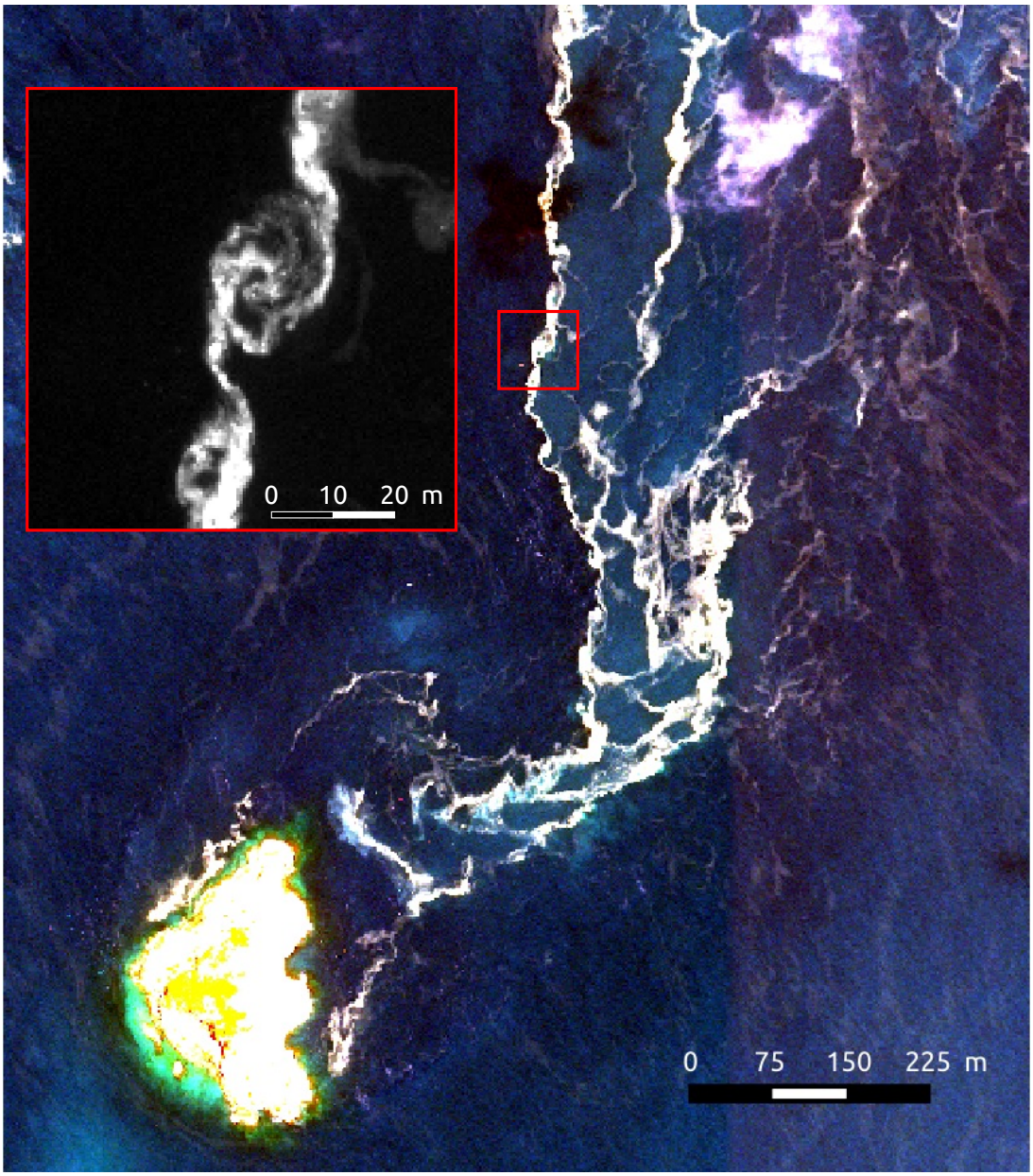

Fig. 11 Small eddies in the free shear layer downstream of Renou Island, located on the east side of gap A (Fig. 3). Inset shows 0.5 m resolution panchromatic imagery within a zoomed area (red box). The pan data reveal clockwise swirls of algae, consistent with shear-induced eddies of about 10-m diameter.

References

Beaman R (2010) Project 3DGBR: A high-resolution depth model for the Great Barrier Reef and Coral Sea. Marine and Tropical Sciences Research Facility (MTSRF) Project 2.5 i. 1a Final Report. Reef and Rainforest Research Centre, Cairns, Australia p pp13 & Appendix 1

Caldeira RMA, Sangrà P (2012) Complex geophysical wake flows. Ocean Dynamics 62(5):683–700

Carrere L, Lyard F, Cancet M, Guillot A (2015) FES 2014, a new tidal model on the global ocean with enhanced accuracy in shallow seas and in the Arctic region. In: EGU General Assembly Conference Abstracts, vol 17, p 5481

Chen W (2011) Nonlinear inverse model for velocity estimation from an image sequence. Journal of Geophysical Research: Oceans 116(C6)

Coutis P, Middleton J (2002) The physical and biological impact of a small island wake in the deep ocean. Deep Sea Research Part I: Oceanographic Research Papers 49(8):1341–1361

Critchell K, Lambrechts J (2016) Modelling accumulation of marine plastics in the coastal zone; what are the dominant physical processes? Estuarine, Coastal and Shelf Science 171:111–122

Critchell K, Grech A, Schlaefer J, Andutta F, Lambrechts J, Wolanski E, Hamann M (2015) Modelling the fate of marine debris along a complex shoreline: Lessons from the Great Barrier Reef. Estuarine, Coastal and Shelf Science 167:414–426

Dam G, Bliek A, Labeur R, Ides S, Plancke Y (2007) Long term process-based morphological model of the Western Scheldt Estuary. In: Proceedings of 5th IAHR symposium of the River, Coastal and Estuarine Morphodynamics Conference, Enschede, The Netherlans (Dohmen-Janssen CM and Hulscher SJMH (eds)), Taylor & Francis, Leiden, The Netherlands, vol 2, pp 1077–1084

Delandmeter P, Lewis SE, Lambrechts J, Deleersnijder E, Legat V, Wolanski E (2015) The transport and fate of riverine fine sediment exported to a semi-open system. Estuarine, Coastal and Shelf Science 167:336–346

Deleersnijder E (2016) Some thoughts on diagnoses for eddies in the Great Barrier Reef, Australia. URL http://hdl.handle.net/2078.1/169841, Université catholique de Louvain, working note, 26 pages

Dong C, McWilliams JC (2007) A numerical study of island wakes in the Southern California Bight. Continental Shelf Research 27(9):1233–1248

Egbert GD, Erofeeva SY (2002) Efficient inverse modeling of barotropic ocean tides. Journal of Atmospheric and Oceanic Technology 19(2):183–204

Eliassen IK, Heggelund Y, Haakstad M (2001) A numerical study of the circulation in Saltfjorden, Saltstraumen and Skjerstadfjorden. Continental Shelf Research 21(15):1669–1689

Falconer RA, Wolanski E, Mardapitta-Hadjipandeli L (1986) Modeling tidal circulation in an island's wake. Journal of Waterway, Port, Coastal, and Ocean Engineering 112(2):234–254

Furnas M (1992) Pelagic Trichodesmium (= Oscillatoria) in the Great Barrier Reef region. In: Marine Pelagic Cyanobacteria: Trichodesmium and other Diazotrophs, Springer, pp 265–272

Grech A, Wolter J, Coles R, McKenzie L, Rasheed M, Thomas C, Waycott M, Hanert E (2016) Spatial patterns of seagrass dispersal and settlement. Diversity and Distributions 22(11):1150–1162

Hamann M, Grech A, Wolanski E, Lambrechts J (2011) Modelling the fate of marine turtle hatchlings. Ecological Modelling 222(8):1515–1521

Hammer W, Hauri I (1977) Fine-scale surface currents in the Whitsunday Islands, Queensland, Australia: effect of tide and topography. Marine and Freshwater Research 28(3):333–359

Hanert E (2004) Towards a Finite Element Ocean Circulation Model. PhD thesis, Université catholique de Louvain

Huang Z, Ferré J, Kawall J, Keffer J (1995) The connection between near and far regions of the turbulent porous body wake. Experimental thermal and fluid science 11(2):143–154

Jones JE, Davies AM (2008) Storm surge computations for the west coast of Britain using a finite element model (TELEMAC). Ocean Dynamics 58(5-6):337–363

Kingsford M, Wolanski E (2008) Oceanography. In: Hutchings PA, Hoegh-Guldberg O (eds) The Great Barrier Reef: biology, environment and management, vol 2, Csiro publishing and Springer, Collingwood and Dordrecht, pp 28–39

Lambrechts J, Hanert E, Deleersnijder E, Bernard PE, Legat V, Remacle JF, Wolanski E (2008) A multi-scale model of the hydrodynamics of the whole Great Barrier Reef. Estuarine, Coastal and Shelf Science 79(1):143–151

Lambrechts J, Humphrey C, McKinna L, Gourge O, Fabricius K, Mehta A, Lewis S, Wolanski E (2010) Importance of wave-induced bed liquefaction in the fine sediment budget of Cleveland Bay, Great Barrier Reef. Estuarine, Coastal and Shelf Science 89(2):154–162

Le Bars Y, Vallaeys V, Deleersnijder E, Hanert E, Carrere L, Channelière C (2016) Unstructured-mesh modeling of the Congo river-to-sea continuum. Ocean Dynamics 66(4):589–603

Legrand S, Deleersnijder E, Hanert E, Legat V, Wolanski E (2006) High-resolution, unstructured meshes for hydrodynamic models of the Great Barrier Reef, Australia. Estuarine, coastal and shelf science 68(1):36–46

Lyard F, Lefevre F, Letellier T, Francis O (2006) Modelling the global ocean tides: modern insights from FES2004. Ocean Dynamics 56(5-6):394–415

Mantovanelli A, Heron M, Heron S, Steinberg C (2012) Relative dispersion of surface drifters in a barrier reef region. Journal of Geophysical Research: Oceans 117(C11)

Mao Y, Luick JL (2014) Circulation in the southern Great Barrier Reef studied through an integration of multiple remote sensing and in situ measurements. Journal of Geophysical Research: Oceans 119(3):1621–1643

McKinna LI (2015) Three decades of ocean-color remote-sensing Trichodesmium spp. in the Worlds oceans: A review. Progress in Oceanography 131:177–199

McKinna LI, Furnas MJ, Ridd PV (2011) A simple, binary classification algorithm for the detection of Trichodesmium spp. within the Great Barrier Reef using MODIS imagery. Limnol Oceanogr Methods 9(2):50–66

Munday DR, Marshall DP, Piggott MD (2010) Idealised flow past an island in a dynamically adaptive finite element model. Ocean dynamics 60(4):835–850

Nakano M (1957) On the Eddies of Naruto Strait. Papers in Meteorology and Geophysics 7(4):425–434

Obst BS, Hamner WM, Hamner PP (1996) Kinematics of phalarope spinning. Nature 384:121

Onishi S (1984) Study of vortex structure in water surface jets by means of remote sensing. Elsevier oceanography series 38:107–132

Onishi S, Nishimura T (1980) Study on Vortex Current in Strait With Remote-Sensing. Coastal Engineering Proceedings 1(17)

Pham Van C, Deleersnijder E, Bousmar D, Soares-Frazao S (2014) Simulation of flow in compound open-channel using a discontinuous Galerkin finite-element method with Smagorinsky turbulence closure. Journal of Hydro-environment Research 8(4):396–409

Robinson AR (2012) Eddies in marine science. Springer Science & Business Media

Saha S, Moorthi S, Pan HL, Wu X, Wang J, Nadiga S, Tripp P, Kistler R, Woollen J, Behringer D, et al. (2010) The NCEP climate forecast system reanalysis. Bulletin of the American Meteorological Society 91(8):1015

Sakamoto H, Tan K, Haniu H (1991) An optimum suppression of fluid forces by controlling a shear layer separated from a square prism. Journal of fluids engineering 113:183

Signell RP, Geyer WR (1991) Transient eddy formation around headlands. J Geophys Res 96(C2):2561–2575

Smagorinsky J (1963) General circulation experiments with the primitive equations: I. the basic experiment. Monthly Weather Review 91(3):99–164

Strykowski P, Sreenivasan K (1990) On the formation and suppression of vortex 'shedding' at low reynolds numbers. Journal of Fluid Mechanics 218:71–107

Thomas CJ, Lambrechts J, Wolanski E, Traag VA, Blondel VD, Deleersnijder E, Hanert E (2014) Numerical modelling and graph theory tools to study ecological connectivity in the Great Barrier Reef. Ecological Modelling 272:160–174

Thomas CJ, Bridge TC, Figueiredo J, Deleersnijder E, Hanert E (2015) Connectivity between submerged and near-sea-surface coral reefs: can submerged reef populations act as refuges? Diversity and Distributions 21(10):1254–1266

Tseng Q, Duchemin-Pelletier E, Deshiere A, Balland M, Guillou H, Filhol O, Théry M (2012) Spatial organization of the extracellular matrix regulates cell–cell junction positioning. Proceedings of the National Academy of Sciences 109(5):1506–1511

White L, Wolanski E (2008) Flow separation and vertical motions in a tidal flow interacting with a shallow-water island. Estuarine, Coastal and Shelf Science 77(3):457–466

Wolanski E (1993) Facts and numerical artefacts in modelling the dispersal of crown-of-thorns starfish larvae in the Great Barrier Reef. Marine and Freshwater Research 44(3):427–436

Wolanski E (1994) Physical oceanographic processes of the Great Barrier Reef. CRC Press

Wolanski E (2016) Bounded and unbounded boundaries–Untangling mechanisms for estuarine-marine ecological connectivity: Scales of m to 10,000 km–A review. Estuarine, Coastal and Shelf Science

Wolanski E, Elliott M (2015) Estuarine Ecohydrology: an Introduction, 2nd ed. Elsevier, Amsterdam, 322 pp

Wolanski E, Hamner W (1988) Topographically controlled fronts in the ocean and their biological influence. Science 241:177–181

Wolanski E, Kingsford MJ (2014) Oceanographic and behavioural assumptions in models of the fate of coral and coral reef fish larvae. Journal of The Royal Society Interface 11(98):20140,209

Wolanski E, Imberger J, Heron M (1984) Island wakes in shallow coastal waters. Journal of Geophysical Research 89(C6):10,553–10,569

Wolanski E, Asaeda T, Tanaka A, Deleersnijder E (1996) Three-dimensional island wakes in the field, laboratory experiments and numerical models. Continental Shelf Research 16(11):1437–1452

Wolanski E, Brinkman R, Spagnol S, McAllister F, Steinberg C, Skirving W, Deleersnijder E (2003) Merging scales in models of water circulation: perspectives from the Great Barrier Reef. Elsevier Oceanography Series 67:411–429

Young I, Black K, Heron M (1994) Circulation in the ribbon reef region of the Great Barrier Reef. Continental Shelf Research 14(2):117–142